Two-dimensional conical dispersion in $ZrTe_5$ evidenced by optical spectroscopy

E. Martino,[1,*] I. Crassee,[2,*] G. Eguchi,[3] D. Santos-Cottin,[4] R.D. Zhong,[5] G.D. Gu,[5] H. Berger,[1] Z. Rukelj,[6] M. Orlita,[7,8] C. C. Homes,[5] and Ana Akrap[4,†]

[1] *IPHYS, EPFL, CH-1015 Lausanne, Switzerland*
[2] *LNCMI, CNRS-UGA-UPS-INSA, 25, avenue des Martyrs, F-38042 Grenoble, France*
[3] *Institute of Solid State Physics, Vienna University of Technology, Wiedner Hauptstrasse 8-10, 1040 Vienna, Austria*
[4] *Department of Physics, University of Fribourg, Chemin du Musée 3, CH-1700 Fribourg, Switzerland*
[5] *Condensed Matter Physics and Materials Science Department, Brookhaven National Laboratory, Upton, New York 11973, USA*
[6] *Department of Physics, Faculty of Science, University of Zagreb, Bijenička 32, HR-10000 Zagreb, Croatia*
[7] *LNCMI, CNRS-UGA-UPS-INSA-EMFL, 25, avenue des Martyrs, F-38042 Grenoble, France*
[8] *Institute of Physics, Charles University in Prague, CZ-12116 Prague, Czech Republic*

(Dated: August 20, 2021)

Zirconium pentatelluride was recently reported to be a 3D Dirac semimetal, with a single conical band, located at the center of the Brillouin zone. The cone's lack of protection by the lattice symmetry immediately sparked vast discussions about the size and topological/trivial nature of a possible gap opening. Here we report on a combined optical and transport study of $ZrTe_5$, which reveals an alternative view of electronic bands in this material. We conclude that the dispersion is approximately linear only in the *a*-*c* plane, while remaining relatively flat and parabolic in the third direction (along the *b* axis). Therefore, the electronic states in $ZrTe_5$ cannot be described using the model of 3D Dirac massless electrons, even when staying at energies well above the band gap $2\Delta = 6$ meV found in our experiments at low temperatures.

In materials with topological phases, small energy scales can play an important role. $ZrTe_5$ is an excellent example. The band gap opening at the center of the Brillouin zone is caused by a strong spin orbit interaction [1], making the gap topological, be it positive, zero, or negative. $ZrTe_5$ is a layered compound with an extremely high mobility, and there is consensus in scientific literature that the low energy bands in $ZrTe_5$ are conical [2–7]. However, the delicate balance of these energy scales has led to many contradicting reports. Several possible topological phases were predicted or reported in $ZrTe_5$, amongst them a quantum spin Hall insulator [1], weak topological insulator (WTI) [8], strong TI (STI) [9–11], and a three-dimensional (3D) Dirac semimetal [5, 6]. All of these possible phases are linked to a key question: What is the true dimensionality of the conical dispersion in $ZrTe_5$? The detailed band structure has not yet been established, nor is it known whether the linear dispersion is indeed three-dimensional. Band structure calculations critically depend upon fine structural details [12]. ARPES measurements have shown linearly dispersing bands in the *a*-*c* planes, and a strongly varying chemical potential as a function of temperature [3, 4]. It is an open question how the shift of chemical potential measured at the surface relates to the bulk properties, and what the dispersion in the out-of-plane direction is.

In this work, we demonstrate a two-dimensional conical dispersion, and show the temperature-induced shift of the chemical potential across the gap in $ZrTe_5$. Our findings are based on bulk-sensitive techniques, optical spectroscopy and magneto-transport. We address low-energy states due to low carrier density in our samples. We show that the free-carrier optical plasmon energy depends non-monotonically on temperature. The sign of the dominant carriers changes from high-temperature thermally-activated holes to low-temperature electrons. Most importantly, we find that the energy dispersion cannot be linear in all three directions. Rather, our optical conductivity points to a linear dispersion in the *a*-*c* plane, and a parabolic dispersion along the *b* axis. We construct an effective Hamiltonian explaining both the optical and transport properties at low temperatures. Our results place a strong doubt over the commonly accepted picture of a 3D Dirac dispersion.

Measurements were performed on samples synthesized by two different methods, self-flux growth [2] (sample A) and chemical vapor transport [13] (sample B), leading to different low-temperature carrier concentrations. The transport properties are measured using a custom setup. The magneto-transport data are obtained using Quantum Design PPMS. Optical reflectance is measured using FTIR spectroscopy, with *in situ* gold evaporation [14]. At high energies, the phase was fixed by ellipsometry. We use Kramers-Kronig relations to obtain the frequency-dependent complex dielectric function $\epsilon(\omega)$, where ω is the incident photon frequency. Magneto-transmission was measured using a superconducting coil, with sample at $T = 2$ K in a low-pressure helium exchange gas. Analysis of the optical spectra was performed using RefFIT software [15].

The orthorhombic structure of $ZrTe_5$ is shown in Fig. 1(a). The most conducting direction is the *a* axis, running along the Zr chains. The layers are stacked along the least conducting *b* direction. The conduction and va-

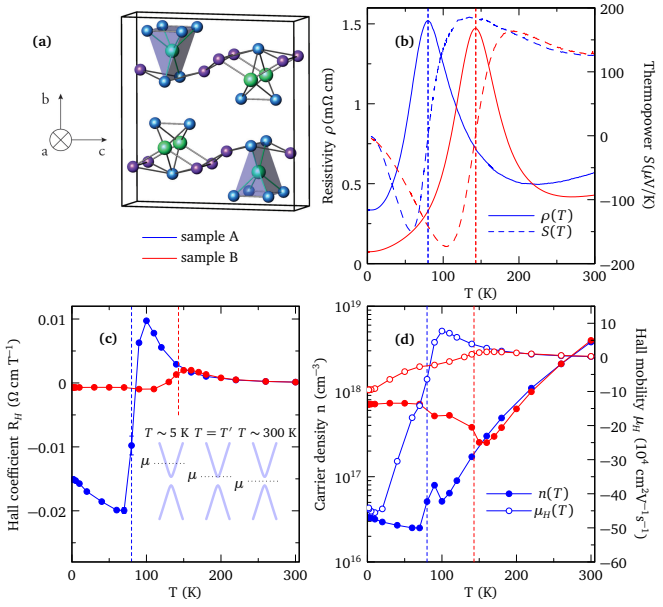

FIG. 1. (color online) (a) Orthorhombic unit cell of $ZrTe_5$. (b) Resistivity and thermoelectric power, (c) Hall coefficient, (d) carrier density and Hall mobility are shown for samples A and B. Blue and red dashed vertical lines denote temperatures T'_A and T'_B, respectively. Inset in (c) illustrates the chemical potential shift with temperature.

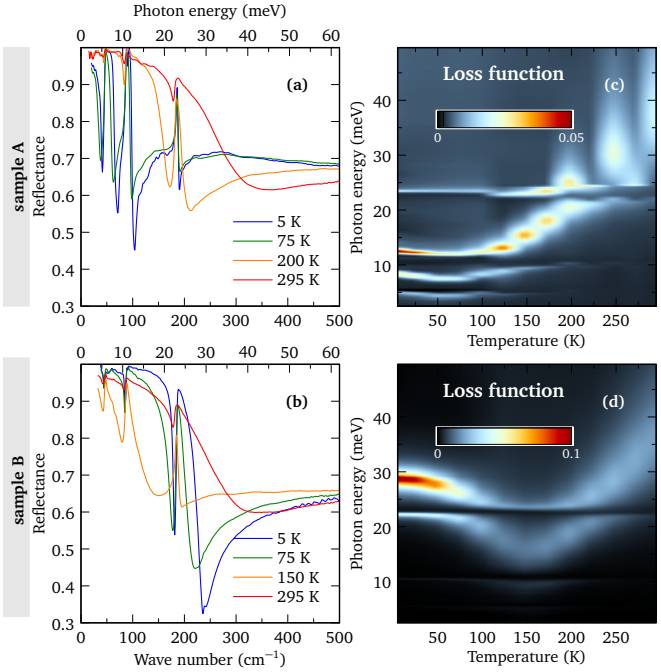

FIG. 2. (color online) Reflectance of (a) sample A and (b) sample B as a function of photon energy. Loss function colormap for (b) sample A and (d) sample B. The data was taken at each 25K, and interpolated.

lence bands are based upon the tellurium p orbitals. Figure 1(b–d) shows electronic transport along the a axis for samples A and B. Panel (b) shows resistivity ρ and thermoelectric power S, (d) Hall coefficient R_H, (e) single band carrier density n, and Hall mobility μ_H, each as a function of temperature. A dramatic change occurs in each quantity at temperature T'; $T'_A = 80$ K for sample A, and $T'_B = 145$ K for sample B. These temperatures correspond to a maximum in ρ, a sign inversion in S, R_H and μ_H, and a minimum in n. The resistivity peak appears to be linked to a minimum in carrier density at T', with a concomitant crossover from electron to hole-dominated conduction.

The metallic resistivity well below T' is described by $\rho = \rho_0 + AT^2$, with $A_A = 0.1$ $\mu\Omega$cm/K^2 and $A_B = 0.036$ $\mu\Omega$cm/K^2 for sample A and sample B, respectively. The coefficient A is inversely proportional to E_F [16], indicating that the Fermi level in sample A is lower than in sample B. The Mott formula $S(T) = k_B^2 T/(eE_F)$ gives an estimate of the low-temperature Fermi levels for samples A and B, $E_F^A \sim 14$ meV and $E_F^B \sim 23$ meV. The lower Fermi level in sample A is consistent with a lower carrier density (Fig. 1(e)). The Hall coefficient, carrier density, and Hall mobility are obtained in a single band analysis in the $B \to 0$ limit. They strongly differ for the two samples below T'. In sample A, the mobility at 2 K is extremely high: $\mu_H^A = 0.45 \times 10^6$ cm^2/(Vs), whereas the carrier density is $n_A = 3 \times 10^{16}$cm^{-3}, surprisingly low for a metallic system. A two-band model [17, 18] shows that minority carriers contribute very little to low-temperature conductivity. However, close to T' a two-band picture is needed.

Above 180 K, S, R_H, n and μ_H are similar in both samples, suggesting that the thermally activated carriers dominate at high temperatures. At room temperature, both samples show weakly metallic resistivity, while thermopower is activated, $S = C + 2\Delta/(eT)$, giving a band gap of $2\Delta \sim 20$ meV at high temperature for both samples (C is a constant offset). The chemical potential is therefore within the gap at high temperature. Its temperature evolution is illustrated by the inset in Fig. 1(c); T' depends on the low-temperature carrier density. A small band gap and a steep band dispersion may lead to a strong shift of chemical potential, consistent with linear dispersion.

We have identified the maximum in the resistivity with the minimum in the carrier density. However, resistivity also depends on the scattering rate. To show that it is the carrier density, and not the scattering mechanism, which dominantly drives the resistivity maximum, one can determine the optical properties. The reflectance plasma edge ω_p is linked to the carrier concentration, $\omega_p^2 \propto n/m$, and does not depend on the scattering rate.

The reflectance and loss function are shown in Fig. 2 High reflectance at low energies ($R \to 1$ as $\omega \to 0$) is followed by a sharp drop at the plasma edge. The room-temperature reflectance looks very similar in samples A

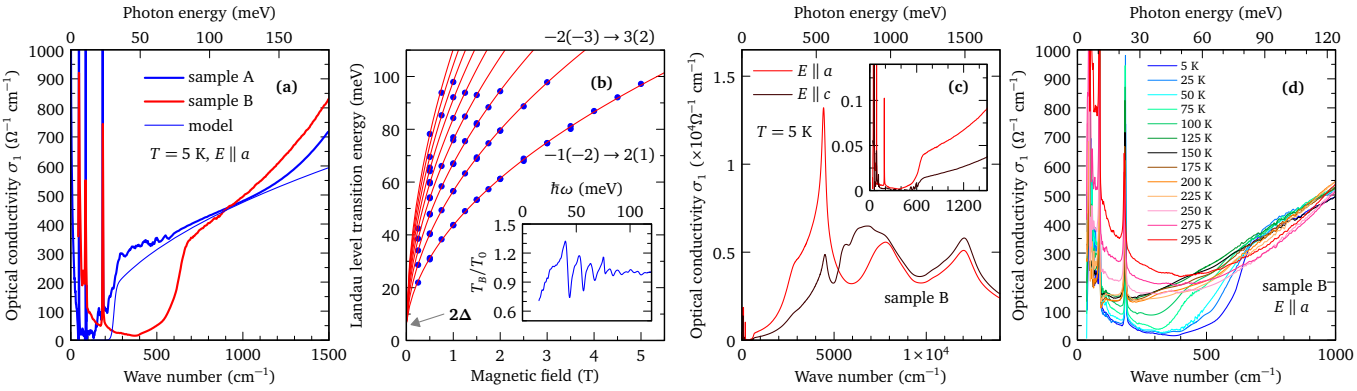

FIG. 3. (color online) (a) $\sigma_1(\omega)$ is shown at 5 K for $E \parallel a$, the calculated conductivity ($\sim \sqrt{\omega}$) is detailed in the text. (b) Landau level transition energies obtained from magneto-optical transmission measurements on sample A, at $T = 2$ K. Red lines are a fit to Eq. 4; the gap $2\Delta = 6$ meV is indicated. The two lowest observed transitions are labeled. Inset shows a relative magneto-transmission spectrum for $B = 1$ T. (c) Wide frequency range $\sigma_1(\omega)$ for the two polarizations in the a-c plane, at $T = 5$ K; inset shows low-energy details of σ_1. (d) Temperature evolution of $\sigma_1(\omega)$ for $E \parallel a$.

and B, with a broad plasma minimum at 45 meV, confirming that the carriers are thermally activated at high temperatures. At low temperatures, the plasma edge in sample A is lower and the phonon-related features are much more pronounced, consistent with a lower carrier density and poorer screening. The plasma edge is lower at 75 K than at 5 K, signifying there is a loss of itinerant carriers as temperature increases from 5 to 75 K. Similarly, in sample B, the plasma edge is the lowest for $T \simeq 150$ K.

The non-monotonic change in carrier density can be visualized better by plotting the loss function, defined as $-\mathrm{Im}(1/\tilde{\epsilon})$, showing the collective modes as peaks. The itinerant carrier plasmon appears as a strong peak with a non-monotonic temperature dependence (Fig. 2(c-d)), with minima at T'_A and T'_B for samples A and B. The loss function also shows three phonon plasmons, visible as horizontal lines in Fig. 2(c). Overall, the reflectance and loss function firmly establish that the carrier density changes non-monotonically with temperature in bulk $ZrTe_5$, in full agreement with the temperature dependence of the carrier density in Fig. 1(e). The peak in $\rho(T)$ is therefore intimately linked to the local minimum in $n(T)$. The same effect is seen in samples with more than an order of magnitude difference in carrier density.

The optical conductivity is related to the dielectric function by $\sigma(\omega) = -2\pi i\omega[\epsilon(\omega) - \epsilon_\infty]/Z_0 = \sigma_1(\omega) + i\sigma_2(\omega)$, where $Z_0 \approx 377\,\Omega$ is the impedance of free space. The real part of optical conductivity, $\sigma_1(\omega)$, is shown in Fig. 3(a) for samples A and B at 5 K, for light polarized along the a axis. The optical conductivity is dominated by a sharp Pauli blocking edge; interband transitions are allowed only when the incident photon energy is higher than the optical gap $2\varepsilon_F$, with Fermi level ε_F measured from the band gap middle. The lower onset of interband absorption in sample A, than in sample B, is consistent with the lower ε_F in sample A. The optical gap is $2\varepsilon_F = 28$ meV in sample A, and 74 meV in sample B. The band gap was determined using magneto-optical transmission measurements, giving $2\Delta = 6$ meV. As discussed below, this band gap is deduced from a small, but well-defined deviation of the interband inter-Landau level transitions from a $\sqrt{B}$ dependence, which is otherwise typical of massless (gapless) charge carriers. This points to a linear dispersion in the a-c plane, in agreement with previous work [6, 10, 19].

TABLE I. Hall mobility, Hall carrier density, effective (cyclotron) mass, optical gap $2\varepsilon_F$, and ε_F/v_a^2 at 5 K. Velocity along a axis is $v_a = 6.9 \times 10^5$ m/s.

sample	μ_H (cm^2/(Vs))	n(cm^{-3})	m	$2\varepsilon_F$ (meV)	ε_F/v_a^2
A	4.5×10^5	3×10^{16}	0.0052	28	0.0052
B	1.0×10^5	7×10^{17}	0.0125	74	0.0137

A combined analysis of the optical conductivity and Hall effect data allows us to determine the effective cyclotron masses in both samples. Spectral weight analysis is performed by integrating the Drude part of the conductivity curve up to $\omega^* = 5$ meV, such that at 5 K the Drude contribution falls within the integration limit [17]. The effective a-c plane masses for samples A and B obtained from this analysis are shown in Table I. Importantly, the effective mass of sample A is smaller than for sample B: $m_B \approx 2.5 m_A$. The apparent dependence of the effective mass on the Fermi energy is clear evidence for a non-parabolic dispersion. For a linearly dispersing system, the effective (cyclotron) mass may be defined by ε_F/v_a^2, which is in excellent agreement with m (Table I), and indicates conical dispersion in the a-c plane.

We now want to verify the nature of the linear dispersion. For a 3D conical band, one expects the real

part of optical conductivity to grow linearly with the frequency, $\sigma_1(\omega) = e^2\nu\omega/(12\hbar v_F)$, where ν is the number of nondegenerate cones at the Fermi level [20, 21]. Such dependence is indeed observed for sample B, with a higher optical gap. However, this model fatally fails to explain the optical conductivity of sample A (Fig. 3(a)) with a lower doping, where $\sigma_1(\omega)$ increases quasi-linearly with ω, but with a well-defined offset.

It has been proposed that such an offset may arise from self-energy effects, $\sigma_1(\omega) \propto \omega - 4\Delta$, which may induce a positive or negative band gap 2Δ [22, 23]. Adopting this scenario, our data would imply $2\Delta \sim -50$ meV (Fig. 3(a)). However, this value exceeds, by an order of magnitude, the size of the gap directly measured by magneto-transmission experiments (Fig. 3(b)). Moreover, the gap readout from the magneto-optical data – if indeed due to self-energy effects – would have to be positive.

To explain the linear, but clearly offset optical conductivity, we propose a simple effective Hamiltonian. It differs from the 3D massive Dirac electron model, often used for $ZrTe_5$, but still implies a massive Dirac dispersion in the a-c plane, with a parabolic dispersion around the band gap 2Δ that straightens to a linear dispersion at higher energies. The dispersion along the b direction remains parabolic or Schrödinger-like at all relevant energies:

$$H = \begin{pmatrix} \Delta + \zeta k_b^2 & \hbar v_a k_a - i\hbar v_c k_c \\ \hbar v_a k_a + i\hbar v_c k_c & -\Delta - \zeta k_b^2 \end{pmatrix}. \quad (1)$$

v_α are the Dirac velocities, and $\zeta = \hbar^2/2m^*$ where m^* is the b-direction effective mass. The eigenvalues of the Hamiltonian are $\varepsilon_{2,1\mathbf{k}} = \pm\sqrt{\hbar^2(v_a k_a)^2 + \hbar^2(v_c k_c)^2 + (\Delta + \zeta k_b^2)^2}$ and they are symmetrical with respect to the band gap middle. The interband conductivity along the a axis can be evaluated in the relaxation constant approximation for $T \approx 0$ [17]

$$\sigma_1^a(\omega) = \frac{e^2}{2\pi\hbar^2}\frac{v_a}{v_c}\sqrt{m^*}\sqrt{\hbar\omega - 2\Delta}\ \Theta(\hbar\omega - 2\varepsilon_F) \quad (2)$$

The ratio $v_a/v_c \approx 1.5$ is determined from the ratio of interband conductivities along the a and c axes (Fig. 3(c)), leaving m^* as the only fitting parameter. The fit shown in Fig. 3(a) gives $m^* \approx 1.8m_e$, and matches the experimental optical conductivity very well, confirming that the dispersion in $ZrTe_5$ is linear in the a-c plane, and parabolic along b direction. Based on the above Hamiltonian, we can determine the total carrier concentration [17]:

$$n = \frac{1}{\pi^2\hbar^3}\frac{1}{v_a v_c}\sqrt{2m^*}\frac{2}{15}(\varepsilon_F - \Delta)^{3/2}(2\Delta + 3\varepsilon_F). \quad (3)$$

Using the value from the Hall effect, $n = 3 \times 10^{16}$ cm^{-3} for sample A, we obtain $v_a = 7.0 \times 10^5$ m/s and $v_c = 4.6 \times 10^5$ m/s, in very good agreement with Shubnikov de Haas experiments [7]. The bare plasmon energy is $\hbar\omega_{pl} = \hbar\sqrt{e^2 n_{aa}/(\epsilon_0 m_e)} = 0.12$ eV, in good agreement with the experimental fit for sample A, 0.1 eV [17]. The energy dispersion may be expanded for small values of k_a, k_b and k_c, since the conduction band is weakly filled. The expansion gives a closed Fermi surface of ellipsoidal shape whose effective masses in various directions are $m_a = \Delta/v_a^2 = 0.001m_e$, $m_c = \Delta/v_c^2 = 0.0025m_e$, and $m_b = m^* = 1.8m_e$. The Landau levels for the Hamiltonian (1) for a magnetic field applied along b axis are [17]

$$\tilde{\varepsilon}(B) = \pm\sqrt{2\hbar e v_a v_c B\mathcal{N} + \Delta^2}. \quad (4)$$

The fit in Fig. 3(b) gives a band gap of $2\Delta = 6$ meV, and the effective Fermi velocity $\sqrt{v_a v_c} = 4.9 \times 10^5$ m/s.

The presence of a band gap in $ZrTe_5$ agrees with the DFT [1, 9, 12, 17], nevertheless, its size appears to be overestimated in these calculations. The DFT favors STI over WTI as a ground state of $ZrTe_5$, both in monolayer and bulk form. Nevertheless, the DFT theory appears to overestimate its size (25-100 meV). Experimentally, the situation is less clear. Both STI and WTI phases have been reported by ARPES or STM/STS [4, 8, 9, 24, 25]. While we do not find direct evidence of either STI or WTI in our experimental data, such a conclusion was made in a recent magneto-optical study [10], reporting on crossing of zero-mode Landau levels, typical of STIs. The DFT studies also indicate [1, 12] that the out-of-plane dispersion is considerably flatter as compared to the in-plane one. This is in line with our findings and the layered nature of $ZrTe_5$. At higher energies, our optical spectra agree with those determined by DFT calculation [17].

Figure 3(d) shows $\sigma_1(\omega)$ for sample B, taken at many different temperatures. As the temperature increases from 5 K to 150 K, the Pauli edge gradually smears out and shifts to lower energies, consistent with the decrease of carrier density. Interestingly, σ_1 appears to be linear in ω at $T = 150$ K. Above 150 K, the low frequency range is filled out by a Drude contribution of the thermally excited carriers which become accessible for $T > 2\Delta/k_B$.

The scattering rate γ for the Drude contribution can be obtained from a Drude-Lorentz modelling of the reflectance [26]. At 5K, for sample A one obtains $\gamma = 1 \pm 1$ meV. The scattering rate can also be extracted from $\sigma_{dc} = e^2 n_{aa}\hbar/(m_e\gamma)$, where n_{aa} is obtained from our model calculation [17]. Here, n_{aa} is the spectral weight of the Drude contribution and is finite irregardless of temperature. This gives $\gamma = 0.5$ meV for sample A, within the error bars of the optically determined scattering rate.

The Hamiltonian (1) may also quantitatively explain the observed T^2 behavior in the resistivity. The T^2 resistivity dependence in a 3D metal is usually caused by three mechanisms: Umklapp scattering, Koshino-Taylor impurity scattering [27, 28], and thermal activation of

carriers. The latter is linked to the temperature dependence of the chemical potential, which is significant in $ZrTe_5$. The electron band properties allow us to calculate the expected coefficient for the sample A, giving two thirds of the fit to the experimental data, $A_A^{calc} \simeq 2/3 A_A$ [17]. All of this points to a fairly good agreement between the model, the optical results, and the transport results.

Finally, Fig. 3(c) shows the optical conductivity in a broad frequency range for both in-plane polarizations, at $T = 5$ K. Several strong features are apparent, and the strongest is at 0.5 eV, which is only ~ 50 meV wide for $E \parallel a$. This feature is a van Hove singularity, due to transitions between flat bands, and it indicates a weaker dispersion along b axis, fully consistent with our Hamiltonian.

In conclusion, $ZrTe_5$ is a fairly simple two-band system of extremes. It has a small band gap, very small effective mass, and may reach extremely low carrier concentration, yet showing metallic conductivity with very high mobility. These specific physical characteristics lead to a chemical potential that strongly shifts as a function of temperature. Crucially, the optical conductivity clearly contradicts the scenario of a 3D cone. Based on the characteristic frequency dependence of $\sigma_1(\omega)$, we conclude that while the dispersion is linear in the a-c plane well above the band gap, it remains parabolic along b axis.

The authors acknowledge illuminating discussions with K. Behnia, B. Fauqué, A.B. Kuzmenko, D. van der Marel, and A. Soluyanov, and kind help by N. Miller. We also thank A. Crepaldi for his generous help with samples, and for extensive discussions. I. C. acknowledges funding from the Postdoc.Mobility fellowship of the Swiss National Science Foundation. A. A. acknowledges funding from the Swiss National Science Foundation through project PP00P2_170544. This work has been supported by the ANR DIRAC3D. We acknowledge the support of LNCMI-CNRS, a member of the European Magnetic Field Laboratory (EMFL). Work at BNL was supported by the U.S. Department of Energy, Office of Basic Energy Sciences, Division of Materials Sciences and Engineering under Contract No. DE-SC0012704.

* These authors contributed equally.
† ana.akrap@unifr.ch

[1] H. Weng, X. Dai, and Z. Fang, Physical Review X **4**, 011002 (2014).
[2] Q. Li, D. E. Kharzeev, C. Zhang, Y. Huang, I. Pletikosić, A. V. Fedorov, R. D. Zhong, J. A. Schneeloch, G. D. Gu, and T. Valla, Nature Physics **12**, 550 EP (2016).
[3] G. Manzoni, A. Sterzi, A. Crepaldi, M. Diego, F. Cilento, M. Zacchigna, P. Bugnon, H. Berger, A. Magrez, M. Grioni, and F. Parmigiani, Physical Review Letters **115**, 207402 (2015).
[4] H. Xiong, J. A. Sobota, S. L. Yang, H. Soifer, A. Gauthier, M. H. Lu, Y. Y. Lv, S. H. Yao, D. Lu, M. Hashimoto, P. S. Kirchmann, Y. F. Chen, and Z. X. Shen, Physical Review B **95**, 195119 (2017).
[5] R. Y. Chen, S. J. Zhang, J. A. Schneeloch, C. Zhang, Q. Li, G. D. Gu, and N. L. Wang, Physical Review B **92**, 075107 (2015).
[6] R. Y. Chen, Z. G. Chen, X. Y. Song, J. A. Schneeloch, G. D. Gu, F. Wang, and N. L. Wang, Physical Review Letters **115**, 176404 (2015).
[7] Y. Liu, X. Yuan, C. Zhang, Z. Jin, A. Narayan, C. Luo, Z. Chen, L. Yang, J. Zou, X. Wu, S. Sanvito, Z. Xia, L. Li, Z. Wang, and F. Xiu, Nature Communications **7**, 12516 EP (2016).
[8] L. Moreschini, J. C. Johannsen, H. Berger, J. Denlinger, C. Jozwiak, E. Rotenberg, K. S. Kim, A. Bostwick, and M. Grioni, Physical Review B **94**, 081101 (2016).
[9] G. Manzoni, L. Gragnaniello, G. Autès, T. Kuhn, A. Sterzi, F. Cilento, M. Zacchigna, V. Enenkel, I. Vobornik, L. Barba, F. Bisti, P. Bugnon, A. Magrez, V. N. Strocov, H. Berger, O. V. Yazyev, M. Fonin, F. Parmigiani, and A. Crepaldi, Physical Review Letters **117**, 237601 (2016).
[10] Z.-G. Chen, R. Y. Chen, R. D. Zhong, J. Schneeloch, C. Zhang, Y. Huang, F. Qu, R. Yu, Q. Li, G. D. Gu, and N. L. Wang, Proceedings of the National Academy of Sciences **114**, 816 (2017).
[11] B. Xu, L. X. Zhao, P. Marsik, E. Sheveleva, F. Lyzwa, Y. M. Dai, G. F. Chen, X. G. Qiu, and C. Bernhard, Physical Review Letters **121**, 187401 (2018).
[12] Z. Fan, Q.-F. Liang, Y. B. Chen, S.-H. Yao, and J. Zhou, Scientific Reports **7**, 45667 EP (2017).
[13] F. Lévy and H. Berger, Journal of Crystal Growth **61**, 61 (1983).
[14] C. C. Homes, M. Reedyk, D. A. Crandles, and T. Timusk, *Applied Optics*, Applied Optics **32**, 2976 (1993).
[15] A. B. Kuzmenko, Review of Scientific Instruments **76**, 083108 (2005).
[16] X. Lin, B. Fauqué, and K. Behnia, Science **349**, 945 (2015).
[17] In the Supplementary Materials we include additional data and theory to support our work, which includes Refs. [29–33].
[18] G. Eguchi and S. Paschen, Physical Review B **99**, 165128 (2019).
[19] Y. Jiang, Z. L. Dun, H. D. Zhou, Z. Lu, K. W. Chen, S. Moon, T. Besara, T. M. Siegrist, R. E. Baumbach, D. Smirnov, and Z. Jiang, Physical Review B **96**, 041101 (2017).
[20] P. Hosur, S. A. Parameswaran, and A. Vishwanath, Phys. Rev. Lett. **108**, 046602 (2012).
[21] A. Bácsi and A. Virosztek, Phys. Rev. B **87**, 125425 (2013).
[22] C. J. Tabert, J. P. Carbotte, and E. J. Nicol, Physical Review B **93**, 085426 (2016).
[23] D. Neubauer, J. P. Carbotte, A. A. Nateprov, A. Löhle, M. Dressel, and A. V. Pronin, Phys. Rev. B **93**, 121202 (2016).
[24] X.-B. Li, W.-K. Huang, Y.-Y. Lv, K.-W. Zhang, C.-L. Yang, B.-B. Zhang, Y. B. Chen, S.-H. Yao, J. Zhou, M.-H. Lu, L. Sheng, S.-C. Li, J.-F. Jia, Q.-K. Xue, Y.-F. Chen, and D.-Y. Xing, Physical Review Letters **116**, 176803 (2016).

[25] R. Wu, J. Z. Ma, S. M. Nie, L. X. Zhao, X. Huang, J. X. Yin, B. B. Fu, P. Richard, G. F. Chen, Z. Fang, X. Dai, H. M. Weng, T. Qian, H. Ding, and S. H. Pan, Physical Review X **6**, 021017 (2016).
[26] A. B. Kuzmenko, Review of Scientific Instruments **76**, (2005).
[27] S. Koshino, Progress of Theoretical Physics **24**, 484 (1960).
[28] P. L. Taylor, Physical Review **135**, A1333 (1964).
[29] D. J. Singh, *Planewaves, Pseudopotentials and the LAPW method* (Kluwer Adademic, Boston, 1994).
[30] D. Singh, Phys. Rev. B **43**, 6388 (1991).
[31] P. Blaha, K. Schwarz, G. K. H. Madsen, D. Kvasnicka and J. Luitz, WIEN2k, *An augmented plane wave plus local orbitals program for calculating crystal properties* (Techn. Universität Wien, Austria, 2001).
[32] S. Furuseth, L. Brattås, and A. Kjekshus, Acta Chem. Scand. **27**, 2367 (1973).
[33] C. Ambrosch-Draxl and J. O. Sofo, Comp. Phys. Commun. **175**, 1 (2006).

Supplementary material for "Two-dimensional conical dispersion in $ZrTe_5$ evidenced by optical spectroscopy"

E. Martino,[1,*] I. Crassee,[2,*] G. Eguchi,[3] D. Santos-Cottin,[4] R.D. Zhong,[5] G.D. Gu,[5] H. Berger,[6] Z. Rukelj,[7] M. Orlita,[8,9] C. C. Homes,[5] and Ana Akrap[4,†]

[1] *IPHYS, EPFL, CH-1015 Ecublens, Switzerland*
[2] *LNCMI, CNRS-UGA-UPS-INSA, 25, avenue des Martyrs, F-38042 Grenoble, France*
[3] *Institute of Solid State Physics, Vienna University of Technology, Wiedner Hauptstrasse 8-10, 1040 Vienna, Austria*
[4] *University of Fribourg, Switzerland*
[5] *Condensed Matter Physics and Materials Science Department, Brookhaven National Laboratory, Upton, New York 11973, USA*
[6] *EPFL, CH-1015 Ecublens, Switzerland*
[7] *Department of Physics, Faculty of Science, University of Zagreb, Bijenička 32, HR-10000 Zagreb, Croatia*
[8] *LNCMI, CNRS-UGA-UPS-INSA-EMFL, 25, avenue des Martyrs, F-38042 Grenoble, France*
[9] *Institute of Physics, Charles University in Prague, CZ-12116 Prague, Czech Republic*

(Dated: May 1, 2019)

In the Supplementary Materials we show the two-band analysis of the magneto-transport data. We continue with the derivation of the interband conductivity for a 2D Dirac cone with a parabolic z dispersion. We explain the definition of the spectral weight applied in the main text. Further, we present a comparison of the experimental optical conductivity and the conductivity determined from a density functional theory band calculation. Finally, we show how one can determine the optical gap from the reflectance spectrum.

TWO-BAND ANALYSIS OF MAGNETO-TRANSPORT DATA

In the main text we show a single-band analysis of the magneto-transport results on single crystals of $ZrTe_5$. This approach shows that the carrier density varies non-monotonically with temperature. The carrier density is minimal at an intermediate, sample-dependent temperature T', the same temperature at which the sign of the majority carriers switches from high-temperature hole-like to low-temperature electron-like carriers.

The goal here is to show how the total carrier density n, Hall mobility μ_H and the *dc* conductivity σ_{xx} can be decomposed using a carefully controlled two-component analysis. In this picture, the two components are an outcome of the analysis at each temperature, and they are an electron-like band and a hole-like band, separated by a band gap of $2\Delta = 6$ meV. The analysis approach is described in the Ref. 1. The results of such a two-component analysis are shown in Fig. S1 (a–c) for sample A, and in panels (d–f) for sample B.

At the lowest temperature ($T = 2$ K), the contribution to the conductivity is dominated by high-mobility electron-like carriers. The minority carriers from the hole-like band contribute very little to the conductivity: less than 1% in sample A, and about 4% in sample B. Similarly, at room temperature, the conductivity is dominated by hole-like carriers. This confirms that at very low temperatures, and at room temperature, a single band is sufficient to describe the transport properties.

In the intermediate range of temperatures, and in particular between 50 and 100 K, the contributions of the two bands become comparable and also more difficult to separate (resulting in larger error bars). Between room temperature and T', the carrier density and the Hall mobility of the majority carriers have a temperature dependence which is characteristic of thermally excited carriers. This is in agreement with the chemical potential being inside the band gap whose size is smaller than the thermal energy of the carriers. The minority component has a weak temperature dependence of the mobility, characteristic of a metallic contribution.

INTERBAND CONDUCTIVITY FOR A 2D DIRAC CONE WITH A PARABOLIC z-DISPERSION

A simple two band Hamiltonian is presented with four free parameters. Optical conductivity, single band density of state and low energy form of the electron dispersions are calculated from the model and used in obtaining values that can be compared to the experimental results. The free parameters of the proposed Hamiltonian can in this way be unambiguously determined.

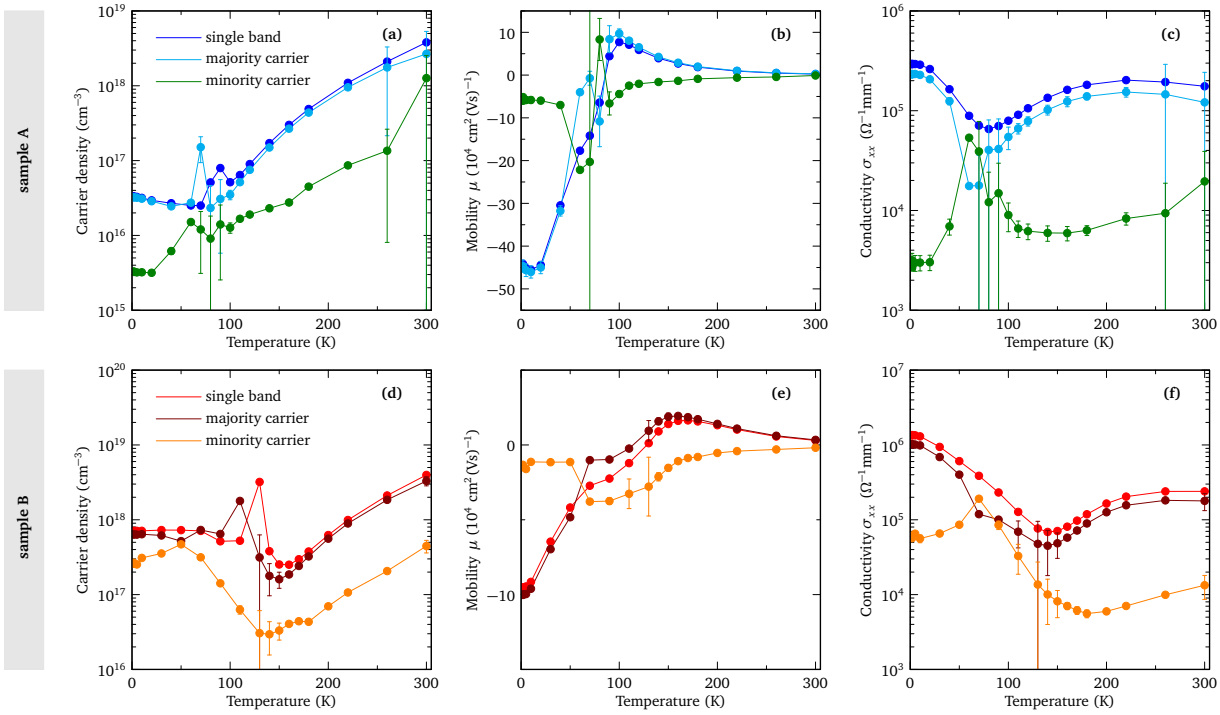

Fig. S1. Carrier density, mobility, and conductivity obtained in a two-band analysis as discussed in the text.

Hamiltonian

Here we present a posible two band electron model with the quasi-Dirac features in the vicinity of the Γ point in the Brillouin zone. It phenomenologically implements the energy band gap 2Δ originating from the spin-orbit coupling, with the assumption of a free-electron like behaviour in the z direction. The Hamiltonian is

$$H = \begin{pmatrix} \Delta + \zeta k_b^2 & \hbar v_a k_a - i\hbar v_c k_c \\ \hbar v_a k_a + i\hbar v_c k_c & -\Delta - \zeta k_b^2 \end{pmatrix}. \tag{S1}$$

The elements v_α are the Dirac velocities in the a and c direction and $\zeta = \hbar^2/2m^*$ with m^* being the effective mass. These parameters can be unambiguously determined by comparing the experimental data from the optical and transport measurement on a clean $ZrTe_5$ sample and the predictions derived from the above Hamiltonian. The eigenvalues of the Hamiltonian (S1) are

$$\varepsilon_{2,1\mathbf{k}} = \pm\sqrt{\hbar^2(v_a k_a)^2 + \hbar^2(v_c k_c)^2 + (\Delta + \zeta k_b^2)^2}. \tag{S2}$$

and are symmetrical to one another with respect to the band gap middle. Since conduction band $\varepsilon_{2\mathbf{k}}$ is weakly filled we can expand (S2) to the $\mathcal{O}(k^2)$

$$\varepsilon_{2\mathbf{k}} \approx \Delta + \frac{(\hbar v_a)^2}{2\Delta}k_a^2 + \frac{(\hbar v_c)^2}{2\Delta}k_c^2 + \frac{\hbar^2}{2m^*}k_b^2, \tag{S3}$$

thus obtaining the effective masses

$$m_{aa} = \Delta/v_a^2,\ m_{cc} = \Delta/v_c^2,\ m_{bb} = m^* \tag{S4}$$

Interband conductivity

The interband conductivity tensor $\sigma^\alpha(\omega, T)$ in the relaxation constant approximation Γ is given in the usual way

$$\sigma^\alpha(\omega, T) = \frac{i\hbar}{V}\sum_{\mathbf{k}\sigma L\neq \underline{L}} \frac{\left|J^{L\underline{L}}_{\alpha\mathbf{k}}\right|^2}{\varepsilon_{\underline{L}\mathbf{k}} - \varepsilon_{L\mathbf{k}}} \frac{f_{L\mathbf{k}} - f_{\underline{L}\mathbf{k}}}{\hbar\omega + \varepsilon_{L\mathbf{k}} - \varepsilon_{\underline{L}\mathbf{k}} + i\Gamma_{\underline{L}L}} \tag{S5}$$

where $\alpha \in \{a, c, b\}$ is a Cartesian coordinate and $J^{LL}_{\alpha\mathbf{k}}$ are the interband current vertices calculated further below. Now we can calculate the interband conductivity in the a direction in the case of vanishing relaxation constant $\Gamma_{12} \to 0$. Using the derived value $|J_{a\mathbf{k}}|^2 = e^2 v_a^2$ and taking only the positive values of $\Omega = \hbar\omega$, the real part of (S5) reduces to

$$\sigma_1^a(\Omega, T) = \hbar e^2 v_a^2 \pi \frac{1}{V} \sum_{\mathbf{k}\sigma} \frac{f_{1\mathbf{k}} - f_{2\mathbf{k}}}{\varepsilon_{2\mathbf{k}} - \varepsilon_{1\mathbf{k}}} \delta(\Omega - \varepsilon_{2\mathbf{k}} + \varepsilon_{1\mathbf{k}}). \tag{S6}$$

The temperature dependence is implemented in the Fermi-Dirac distribution. Taking into account that $\varepsilon_{2\mathbf{k}} = -\varepsilon_{1\mathbf{k}}$ and that the expresion (S6) is finite only for $\Omega = \varepsilon_{2\mathbf{k}} - \varepsilon_{1\mathbf{k}}$, the distribution functions can be written

$$\begin{aligned} F(\Omega, T) = f_{1\mathbf{k}} - f_{2\mathbf{k}} &= \frac{1}{e^{\beta(-\Omega/2-\mu)} + 1} - \frac{1}{e^{\beta(\Omega/2-\mu)} + 1} \\ &= \frac{\mathrm{sh}(\beta\Omega/2)}{\mathrm{ch}(\beta\mu) + \mathrm{ch}(\beta\Omega/2)} \underset{T=0}{\longrightarrow} \Theta(\Omega - 2\varepsilon_F) \end{aligned} \tag{S7}$$

Next, we introduce the new variables $2v_a\hbar k_a = x$, $2v_c\hbar k_c = y$ and $k_b\sqrt{2\zeta} = z$. Thus (S6) becomes

$$\sigma_1^a(\Omega, T) = \frac{\hbar e^2 v_a^2 \pi}{(2\pi)^3} \frac{F(\Omega, T)}{(2v_a\hbar)(2v_c\hbar)} \frac{2}{\sqrt{2\zeta}} \iiint \frac{\delta\left(\Omega - \sqrt{x^2 + y^2 + (2\Delta + z^2)^2}\right)}{\sqrt{x^2 + y^2 + (2\Delta + z^2)^2}} dxdydz \tag{S8}$$

Changing the Cartesian to the cyllindrical system by introducing $\varrho^2 = x^2 + y^2$ (S8) is

$$\sigma_1^a(\Omega, T) = \frac{\hbar e^2 v_a^2 \pi}{(2\pi)^3} \frac{F(\Omega, T)}{(2v_a\hbar)(2v_c\hbar)} \frac{4\pi}{\sqrt{2\zeta}} \int_0^\infty \int_{-\infty}^\infty \frac{\delta\left(\Omega - \sqrt{\varrho^2 + (2\Delta + z^2)^2}\right)}{\sqrt{\varrho^2 + (2\Delta + z^2)^2}} \varrho d\varrho dz \tag{S9}$$

We note that there are two zeros of z argument within the δ function $z_0 = \pm\sqrt{\sqrt{\Omega^2 - \varrho^2} - 2\Delta}$. This gives an extra factor of 2

$$\sigma_1^a(\Omega, T) = \frac{\hbar e^2 v_a^2 \pi}{(2\pi)^3} \frac{F(\Omega, T)}{(2v_a\hbar)} \frac{1}{(2v_c\hbar)} \frac{8\pi}{\sqrt{2\zeta}} \int_0^{\sqrt{\Omega^2 - 4\Delta^2}} \frac{\varrho d\varrho}{\sqrt{\Omega^2 - \varrho^2}\sqrt{\sqrt{\Omega^2 - \varrho^2} - 2\Delta}} \tag{S10}$$

The integral is equal to $2\sqrt{\Omega - 2\Delta}$, giving the final result for the interband conductivity in terms of $\sigma_0 = e^2/(4\hbar)$ for $T = 0$

$$\sigma_1^a(\Omega, 0) = \frac{\sigma_0}{\pi} \frac{v_a}{v_c} \frac{\sqrt{m^*}}{\hbar} \sqrt{\Omega - 2\Delta}\ \Theta(\Omega - 2\varepsilon_F), \tag{S11}$$

The derivation of $\sigma_1^a(\Omega)$ is esentialy the same, the only difference is the current vertex (S37). This gives

$$\sigma_1^c(\Omega, 0) = \frac{\sigma_0}{\pi} \frac{v_c}{v_a} \frac{\sqrt{m^*}}{\hbar} \sqrt{\Omega - 2\Delta}\ \Theta(\Omega - 2\varepsilon_F) \tag{S12}$$

Using (S11) and (S12) we are at liberty to write the second prediction of our model

$$\frac{\sigma_1^a(\Omega, 0)}{\sigma_1^c(\Omega, 0)} = \frac{v_a^2}{v_c^2} \tag{S13}$$

Density of states

The single band density of state is defined

$$g(\varepsilon) = \frac{1}{V} \sum_{\mathbf{k}\sigma} \delta(\varepsilon - \varepsilon_{2\mathbf{k}}) \tag{S14}$$

Using the eigenvalues (S2) and the procedure outlined in (S8)-(S11) we obtain

$$g(\varepsilon) = \frac{1}{\pi^2\hbar^3}\frac{1}{v_a v_c}\sqrt{2m^*}\,\varepsilon\sqrt{\varepsilon-\Delta} \tag{S15}$$

Now, the connection to the concentration of electrons can be made. For $T = 0$ we have

$$n = \int_{\Delta}^{\varepsilon_F} g(\varepsilon)d\varepsilon = \frac{1}{\pi^2\hbar^3}\frac{1}{v_a v_c}\sqrt{2m^*}\frac{2}{15}(\varepsilon_F-\Delta)^{3/2}(2\Delta+3\varepsilon_F). \tag{S16}$$

Effective number of charge carriers and the plasmon frequency

The effective concentration of charge carriers $n_{\alpha\alpha}$ is defined

$$n_\alpha = -\frac{1}{V}\sum_{\mathbf{k}\sigma} m_e v_{\alpha\mathbf{k}}^2 \frac{\partial f_{\mathbf{k}}}{\partial\varepsilon_{\mathbf{k}}}, \tag{S17}$$

where $v_{\alpha\mathbf{k}} = (1/\hbar)\partial\varepsilon_{\mathbf{k}}/\partial k_\alpha$. Choosing $\alpha = a$, for low temperatures ($T \approx 0$) we have $\partial f_{\mathbf{k}}/\partial\varepsilon_{\mathbf{k}} = -\delta(\varepsilon_F - \varepsilon_{\mathbf{k}})$. Using the dispersion (S3) in expression (S17) we have

$$n_a = \frac{1}{(2\pi)^3}2m_e\frac{\hbar^2}{m_{aa}^2}\frac{2m_{aa}}{\hbar^2}\frac{\sqrt{2m_{aa}2m_{cc}2m_{bb}}}{\hbar^3}\iiint x^2\delta(\varepsilon_F-\Delta-x^2-y^2-z^2)dx\,dy\,dz \tag{S18}$$

with the redefined variables $x^2 = (\hbar^2/2m_{aa})k_a^2$, $y^2 = (\hbar^2/2m_{cc})k_c^2$ and $z^2 = (\hbar^2/2m_{bb})k_b^2$. Changing from the Cartesian to the cyllindrical system we obtain

$$n_a = \frac{2}{(2\pi)^3}\frac{m_e}{m_{aa}}\frac{\sqrt{2m_{aa}2m_{cc}2m_{bb}}}{\hbar^3}\int_0^\infty\int_0^{2\pi}\varrho^3\cos^2\varphi\,\delta(\varepsilon_F-\Delta-\varrho^2-z^2)d\varrho\,d\varphi\,dz. \tag{S19}$$

Evaluating the δ function integral in the standard way

$$n_a = \frac{4}{(2\pi)^3}\frac{m_e}{m_{aa}}\frac{\sqrt{2m_{aa}2m_{cc}2m_{bb}}}{\hbar^3}\int_0^{\sqrt{\varepsilon_F-\Delta}}\int_0^{2\pi}\frac{\varrho^3\cos^2\varphi}{\sqrt{\varepsilon_F-\Delta-\varrho^2}}d\varrho\,d\varphi, \tag{S20}$$

gives us the final result

$$n_a = \frac{1}{(2\pi)^2}\frac{4}{3}(\varepsilon_F-\Delta)^{3/2}\frac{m_e}{m_{aa}}\frac{\sqrt{2m_{aa}2m_{cc}2m_{bb}}}{\hbar^3}. \tag{S21}$$

By implementing the effective masses (S4) in (S21) we find the effective concentration of charge carriers

$$n_a = 1.06\times10^{25}\,\mathrm{m}^{-3} \gg n = 3\times10^{22}\,\mathrm{m}^{-3} \tag{S22}$$

to be three orders of magnitude larger than n. In the system with the electron bands described by (S3) one has

$$\frac{n_\alpha}{m_e} = \frac{n}{m_{\alpha\alpha}}. \tag{S23}$$

The bare plasmon energy can now be calculated

$$E_{pl} = \hbar\omega_{pl} = \hbar\sqrt{\frac{e^2 n_a}{\epsilon_0 m_e}} = 0.12\,\mathrm{eV} = 970\,\mathrm{cm}^{-1} \tag{S24}$$

and compared with the conductivity sum rule for sample A.

Finite temperature effects

In metals due to finite temperatures the deviations of the chemical potential μ from ε_F is

$$\mu \approx \varepsilon_F \left[1 - \frac{\pi^2}{6}\frac{(k_BT)^2}{\varepsilon_F}\frac{1}{g(\varepsilon)}\frac{\partial g(\varepsilon)}{\partial \varepsilon}\bigg|_{\varepsilon_F}\right] \tag{S25}$$

or inserting (S15) in (S25)

$$\mu \approx \varepsilon_F \left[1 - \frac{\pi^2(k_BT)^2}{12\varepsilon_F^2}\frac{3\varepsilon_F - 2\Delta}{\varepsilon_F - \Delta}\right]. \tag{S26}$$

This alters the effective concentration (S21) in a trivial way

$$\begin{aligned} n_a(T) &= \frac{1}{(2\pi)^2}\frac{4}{3}(\mu-\Delta)^{3/2}\frac{m_e}{m_{aa}}\frac{\sqrt{2m_{aa}2m_{cc}2m_{bb}}}{\hbar^3} \\ &\approx n_a(0)\left(1 - \frac{\pi^2}{8}\frac{(k_BT)^2}{(\varepsilon_F-\Delta)^2}\frac{3\varepsilon_F - 2\Delta}{\varepsilon_F}\right) \end{aligned} \tag{S27}$$

From the definition of Drude DC conductivity with scattering time τ

$$\rho_a(T) = 1/\sigma_1^a(T) = \frac{m_e}{e^2\tau n_a(T)} \approx \frac{m_e}{e^2\tau n_a(0)}\left(1 + \frac{\pi^2}{8}\frac{(k_BT)^2}{(\varepsilon_F-\Delta)^2}\frac{3\varepsilon_F - 2\Delta}{\varepsilon_F}\right) = \rho_a(0) + AT^2 \tag{S28}$$

with the constant $A = 0.66 \times 10^{-9}\Omega\mathrm{m/K}^2$.

Interband current vertices

In the general form of the 2×2 hamiltonian

$$H = \begin{pmatrix} D_{\mathbf{k}} & t_{\mathbf{k}} \\ t_{\mathbf{k}}^* & Q_{\mathbf{k}} \end{pmatrix} \tag{S29}$$

the current vertices are

$$J_{\alpha\mathbf{k}}^{LL'} = \sum_{\ell\ell'}\frac{e}{\hbar}\frac{\partial H_{\mathbf{k}}^{\ell\ell'}}{\partial k_\alpha}U_{\mathbf{k}}(\ell, L)U_{\mathbf{k}}^*(\ell', L') \tag{S30}$$

where $U_{\mathbf{k}}(\ell, L)$ are the elements of matrix defined as $\mathbf{U}\hat{H}\mathbf{U}^{-1} = \mathbf{E}$ and are explicitly given

$$U_{\mathbf{k}}(\ell, L) = \begin{pmatrix} e^{i\varphi_{\mathbf{k}}}\cos(\vartheta_{\mathbf{k}}/2) & e^{i\varphi_{\mathbf{k}}}\sin(\vartheta_{\mathbf{k}}/2) \\ -\sin(\vartheta_{\mathbf{k}}/2) & \cos(\vartheta_{\mathbf{k}}/2) \end{pmatrix} \tag{S31}$$

with the definitions

$$t_{\mathbf{k}} = |t_{\mathbf{k}}|e^{i\varphi_{\mathbf{k}}}, \quad \tan\varphi_{\mathbf{k}} = \frac{\Im t_{\mathbf{k}}}{\Re t_{\mathbf{k}}}, \quad \tan\vartheta_{\mathbf{k}} = \frac{2|t_{\mathbf{k}}|}{D_{\mathbf{k}} - Q_{\mathbf{k}}}. \tag{S32}$$

Therefore in the general case of (S29), equation (S30) gives

$$\frac{\hbar}{e}J_{\alpha\mathbf{k}}^{12} = \frac{\tan\vartheta_{\mathbf{k}}}{2\sqrt{1+\tan^2\vartheta_{\mathbf{k}}}}\frac{\partial(D_{\mathbf{k}} - Q_{\mathbf{k}})}{\partial k_\alpha} + i|t_{\mathbf{k}}|\frac{\partial\varphi_{\mathbf{k}}}{\partial k_\alpha} + \frac{1}{\sqrt{1+\tan^2\vartheta_{\mathbf{k}}}}\frac{\partial|t_{\mathbf{k}}|}{\partial k_\alpha} \tag{S33}$$

Let us now determine the above derivations for the Hamiltonian (S1). We obtain

$$\frac{\partial|t_{\mathbf{k}}|}{\partial k_\alpha} = \hbar\frac{v_a^2k_a\delta_{\alpha,a} + v_c^2k_c\delta_{\alpha,c}}{\sqrt{(v_ak_a)^2 + (v_ck_c)^2}} \tag{S34}$$

and

$$\frac{\partial\varphi_{\mathbf{k}}}{\partial k_\alpha} = \frac{v_a v_c(k_a\delta_{\alpha,c} - k_c\delta_{\alpha,a})}{(v_a k_a)^2 + (v_c k_c)^2} \tag{S35}$$

and trivialy

$$\frac{\partial(D_{\mathbf{k}} - Q_{\mathbf{k}})}{\partial k_\alpha} = 4\zeta k_b \delta_{\alpha,b}. \tag{S36}$$

We are interested in the behaviour in the vicinity of the Dirac point. In this case $(k_a, k_c, k_b) \to 0$ and thus $\tan\vartheta_{\mathbf{k}} \to 0/\Delta = 0$. Then inserting (S35) and (S34) in (S33) for the $\alpha = c$ polarization we have

$$J_{c\mathbf{k}} \approx \frac{e(iv_a v_c k_a + v_c^2 k_c)}{\sqrt{(v_a k_a)^2 + (v_c k_c)^2}} \to |J_{c\mathbf{k}}|^2 = e^2 v_c^2. \tag{S37}$$

On similar grounds we obtain for the case $\alpha = a$

$$|J_{a\mathbf{k}}|^2 = e^2 v_a^2. \tag{S38}$$

Slightly more complicated result is obtained for the b direction which gives

$$|J_{b\mathbf{k}}|^2 = 4e^2\zeta^2 \frac{(v_a k_a)^2 + (v_c k_c)^2}{\varepsilon_{\mathbf{k}}^2} \tag{S39}$$

Interaction with magnetic field

We consider the problem of $ZrTe_5$ in uniform magnetic field applied in z direction. We chose the Landau gauge $\mathbf{A} = -By\hat{x}$. It is easy to verify that $\nabla \times \mathbf{A} = B\hat{z}$. The minimal substitution modifies the electron momentum operator $\hat{\mathbf{p}} \to \hat{\mathbf{p}} + e\mathbf{A}$, or by components $\hat{p}_x \to \hat{p}_x + eBy$, $\hat{p}_y \to \hat{p}_y$, $\hat{p}_z \to \hat{p}_z$. Let us write the Hamiltonian (S1) in x, y, z coordinates

$$H = \begin{pmatrix} \Delta + \zeta k_z^2 & \hbar v_x k_x - i\hbar v_y k_y \\ \hbar v_x k_x + i\hbar v_y k_y & -\Delta - \zeta k_z^2 \end{pmatrix}. \tag{S40}$$

Then using de Broglie relation $\mathbf{p} = \hbar\mathbf{k}$ and coordinate representation of the momentum operator, the H_{12} term of (S40) in magnetic field is transformed $H_{12} \to \tilde{H}_{12}$

$$\begin{aligned} H_{12} &= \hbar v_x k_x - i\hbar v_y k_y \\ &= v_x p_x - i v_y p_y \to v_x(p_x - eBy) - i v_y \hbar \frac{\partial}{\partial y} \\ \tilde{H}_{12} &= \hbar\sqrt{v_x v_y}\left(\sqrt{\frac{v_x}{v_y}}k_x - \sqrt{\frac{v_x}{v_y}}\frac{eB}{\hbar}y - \sqrt{\frac{v_y}{v_x}}\frac{\partial}{\partial y}\right) \\ &= \frac{\hbar}{\ell}\sqrt{v_x v_y}\left(\gamma\ell k_x + \frac{\gamma}{\ell}y - \frac{\ell}{\gamma}\frac{\partial}{\partial y}\right), \end{aligned} \tag{S41}$$

where we have defined the length scale $\ell = \sqrt{\hbar/(eB)}$ and ratio $\gamma = \sqrt{v_x/v_y}$. Similar result is derived for $\tilde{H}_{21}$. Let us introduce $\eta = \gamma\ell k_x - (\gamma/\ell)y$, then using the chain rule $\partial_\eta = -(\ell/\gamma)\partial_y$, (S40) is

$$\tilde{H} = \begin{pmatrix} \Delta + \zeta k_z^2 & (\hbar/\ell)\sqrt{v_x v_y}\,(\eta + \partial_\eta) \\ (\hbar/\ell)\sqrt{v_x v_y}\,(\eta - \partial_\eta) & -\Delta - \zeta k_z^2 \end{pmatrix}. \tag{S42}$$

Defining raising $\hat{a}^\dagger = 1/\sqrt{2}\,(\eta - \partial_\eta)$ and lowering $\hat{a} = 1/\sqrt{2}\,(\eta + \partial_\eta)$ operator we write (S42)

$$\tilde{H} = \begin{pmatrix} \Delta + \zeta k_z^2 & (\hbar/\ell)\sqrt{2v_x v_y}\hat{a} \\ (\hbar/\ell)\sqrt{2v_x v_y}\hat{a}^\dagger & -\Delta - \zeta k_z^2 \end{pmatrix}. \tag{S43}$$

Diagonalization of the above Hamiltonian is straight forward, using the definition of the number operator $\hat{a}^\dagger\hat{a} = \mathcal{N}$ we obtain

$$\tilde{\varepsilon}_{B,k} = \pm\sqrt{2\hbar e v_x v_y B\mathcal{N} + (\Delta + \zeta k_z^2)^2}. \tag{S44}$$

SPECTRAL WEIGHT ANALYSIS

In the main text we determine the spectral weight in the following way:

$$SW = \frac{\omega_p^2}{8} = \int_0^{\omega^*} \sigma_1(\omega) d\omega = \frac{\pi N e^2}{2 m^* V}.$$

This quantity is directly related to the effective band mass m^*. To extract the effective mass, we use $SW \times C \times V_u = N_{eff}$ where N_{eff} is the effective carrier concentration per unit cell, $C = 4.26 \times 10^{14}$ and V_u is the unit cell volume in cm^3. The optically determined N_{eff} is related to the Hall carrier density through $n = N_{eff}/V_u \times m^*$. Here N_{eff} is evaluated for $\omega^* = 5$ meV. $N_{eff} = 0.00455$ for sample A, and 0.044 for sample B.

MAGNETO-OPTICAL TRANSMISSION

In the main text, we determine the band gap using magneto-optical transmission measurements which allow us to follow the energies of Landau level transitions energies in function of magnetic field. Measurements were performed on sample A, at $T = 2$ K, and are shown in Fig. S2.

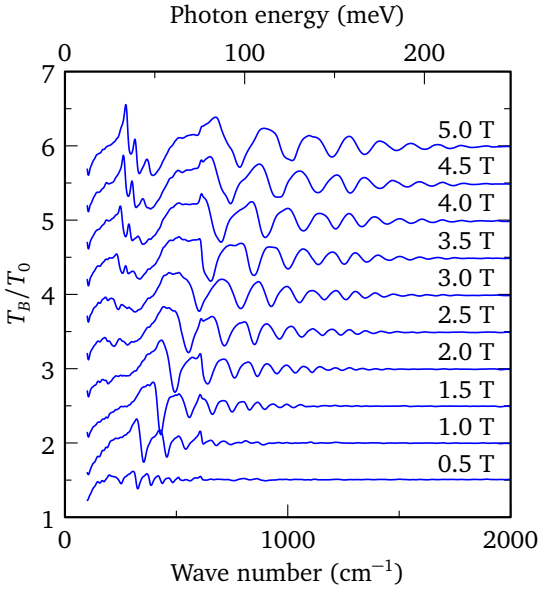

Fig. S2. Magneto-optical transmission for sample A at $T = 2$ K.

OPTICAL CONDUCTIVITY CALCULATED FROM DFT BAND STRUCTURE

The electronic properties of $ZrTe_5$ in the orthorhombic Cmcm (63) phase have been calculated using density functional theory (DFT) with the generalized gradient approximation (GGA) using the full-potential linearized augmented plane-wave (FP-LAPW) method [2] with local-orbital extensions [3] in the WIEN2k implementation [4]. An examination of different Monkhorst-Pack k-point meshes indicated that a $7\times7\times2$ k-point mesh with $R_{mt}k_{max} = 8.25$ was sufficient for good energy convergence. Beginning with the experimental unit cell [5], the total energy was minimized by changing the volume while keeping the c/a ratio constant. The atomic fractional coordinates were then relaxed with respect to the total force, typically resulting in residual forces of less than 0.2 mRy/a.u. per atom. This procedure was repeated until no further improvement was obtained. For both of these procedures spin-orbit coupling is ignored. The final values for the unit cell parameters of $a = 4.06$, $b = 14.76$, and $c = 13.97$ Å are slightly larger than the experimentally-determined values of $a = 3.98$, $b = 14.50$ and $c = 13.72$ Å. The atomic fractional coordinates for Zr, Te1, Te2, and Te3 are determined to be (0.0,0.6847,0.25), (0.0,0.0716,0.1499), (0.0,0.2105,0.5654), and (0.0,0.3352,0.25), respectively,

which are in good agreement with the experimentally-determined values of (0.0,0.6857,0.25), (0.0,0.0701,0.1494), (0.0,0.2099,0.5647), and (0.0,0.3365,0.25).

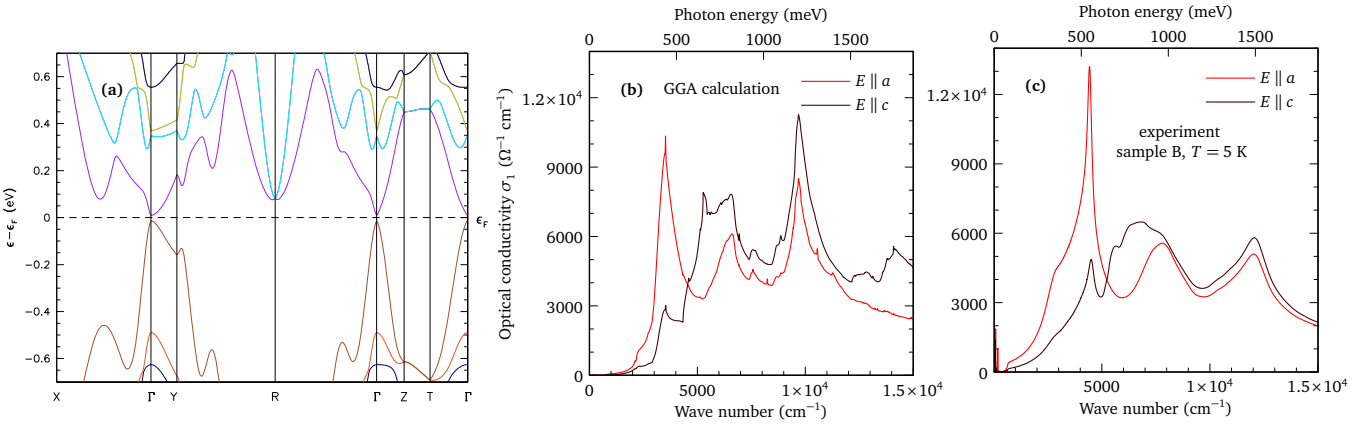

Fig. S3. (a) DFT-calculated band structure in the vicinity of the Fermi level. (b) Optical conductivity determined from the calculated band structure, for the a and c axes. (c) Experimentally determined optical conductivity for light polarized along a and c axes, at $T = 5$K.

The real part of the optical conductivity including the effects of spin orbit coupling has been calculated [6] from the the imaginary part of the dielectric function, $\sigma_{x,x} = 2\pi\omega\,\Im\,\epsilon_{x,x}/Z_0$, using a fine k-point mesh (10 000 k points, yielding a $32\times32\times9$ mesh); $Z_0 \approx 377\,\Omega$ is the impedance of free space, resulting in units for the conductivity of $\Omega^{-1}\text{cm}^{-1}$. In this case, the free-carrier contribution is not calculated, so that the imaginary part of the dielectric function is the sum of the contributions to the dielectric tensor over all the allowed interband transitions. The calculated conductivity is shown along the a and c directions in Fig. S2(a), and is compared to the experimental values at 5 K in Fig. 2(b). The singularities, as well as the general asymmetry in the optical conductivity along the a and c axes are well reproduced, but the peak occurs at a slightly lower energy that is observed experimentally; also, the overall magnitude is lower as well. The conductivity is zero up to about 650 cm^{-1}, above which there is an onset of absorption. This depends on how geometry is optimized. Overall, the calculation agrees very well with the experimental data, both in a and $c-$direction. This means that the singularity at 0.5 eV is indeed van Hove singularity (not excitons for example), and it is two-dimensional.

OPTICAL GAP FROM THE REFLECTANCE DATA

The onset of absorption can be seen directly from the reflectance data, as shown in Fig. S4. The particular measurement shows strong fringes from the Fabry-Perot interference, but only in the transparent regime. The onset of fringes thus corresponds to the onset of absorption at the value of the optical gap or the Pauli blocking. This value also corresponds to half the step in the optical conductivity $\sigma_1(\omega)$. The fringes were observed most likely because that particular sample had split into thin layers during the preparation.

* These authors contributed equally.
† ana.akrap@unifr.ch

[1] G. Eguchi and S. Paschen, Physical Review B **99**, 165128 (2019).
[2] D. J. Singh, *Planewaves, Pseudopotentials and the LAPW method* (Kluwer Adademic, Boston, 1994).
[3] D. Singh, Phys. Rev. B **43**, 6388 (1991).
[4] P. Blaha, K. Schwarz, G. K. H. Madsen, D. Kvasnicka and J. Luitz, WIEN2k, *An augmented plane wave plus local orbitals program for calculating crystal properties* (Techn. Universität Wien, Austria, 2001).
[5] S. Furuseth, L. Brattås, and A. Kjekshus, Acta Chem. Scand. **27**, 2367 (1973).
[6] C. Ambrosch-Draxl and J. O. Sofo, Comp. Phys. Commun. **175**, 1 (2006).

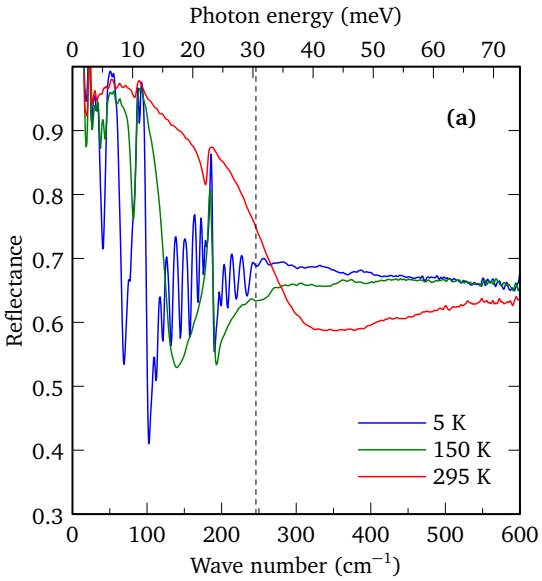

Fig. S4. Optical reflectance showing strong interference fringes, limited to the frequency range below the onset of absorption.